Defect Dynamics in Active Smectics Steered by Extreme Confinement

Zhi-Feng Huang,[1] Hartmut Löwen,[2] and Axel Voigt[3]

[1] *Department of Physics and Astronomy, Wayne State University, Detroit, MI 48201, USA*
[2] *Institut für Theoretische Physik II: Soft Matter, Heinrich-Heine-Universität Düsseldorf, 40225 Düsseldorf, Germany*
[3] *Institute of Scientific Computing, Technische Universität Dresden, 01062 Dresden, Germany*

(Dated: April 4, 2022)

The persistent dynamics in systems out of equilibrium, particularly those characterized by annihilation and creation of topological defects, is known to involve complicated spatiotemporal processes and thus deemed difficult, if even possible, to control. Here the steering of defect dynamics in active smectic layers exposed to extreme confinements is explored, through self-propulsion of active particles and a variety of confining geometries with different topologies. We discover a wealth of dynamical behaviors during the evolution of complex spatiotemporal defect patterns that can be steered by the confining shape and topology, particularly a perpetual creation-annihilation dynamical state with huge fluctuations of topological defects and a transition from oscillatory to damped time correlation of defect number density via the mechanism governed by boundary cusps. Our results are obtained by using an active phase field crystal approach of self-propelled stripes. Possible experimental realizations are also discussed.

Defects in ordered or pattern-forming systems are of great interest both from a fundamental physics point of view highlighting the role of topology in condensed matter [1–3] and for applications since they largely control the material properties. For the example of liquid crystals, most of the studies have focused on topological defects in the orientational ordered nematic phase of lyotropic or thermotropic liquid crystals and by now it has been well understood how to trigger them by external influences [4–8] and confinements [9–14]. In the layered smectic phase, defect characterization is more complex due to the additional positional ordering [15–18] but can be steered by confinement as well [19, 20].

In recent years, active particles that are self-propelled intrinsically and relevant for biological swarms, motor proteins and biofilaments have been of tremendous interest [21–24]. These particles self-organize into fascinating "active" liquid crystalline phases which are qualitatively different from their passive counterparts in or near equilibrium and are governed by nonrelaxational dynamical processes that are the characteristics of far-from-equilibrium pattern-forming or chaotic systems [25]. Due to the internal driving, defect dynamics in active nematics is intriguing with a plethora of new phenomena [26–31]. Also an active smectic-like phase has been examined [32], as modeled by aligning [33] and non-reciprocal [34] interactions or nonlinear feedback [35]. However, our knowledge of defects in active smectics, including their dynamics and controllability by external constraints, is still sparse.

Here we fill this gap and explore defect dynamics of active smectic systems by using an appropriate active phase field crystal (PFC) model [36–43] in the domain where a traveling stripe phase is stable. We expose this state of self-propelled smectics to extreme confinements. A rich variety of geometries with different topologies, including cavities and open or closed channels that are of various convex, concave, and cusped shapes, are considered. A wealth of nonequilibrium defected states are found in the evolution towards complex spatiotemporal patterns arising from a competition of activity and confinement. The corresponding persistent defect dynamics, especially the highly fluctuating creation-annihilation process, goes far beyond the traditional classification familiar in passive systems, and can be steered by the confining shape and topology of the cavity or channel and the degree of particle self-propulsion. In particular, the presence of cuspated boundaries induces or annihilates defects, which can be utilized to control the dynamics of defect creation and the quantitative behavior (oscillatory vs damped) of time correlation of defect density. Our predictions can be verified for confined dense vibrated granular rods [44–46] or self-propelled colloidal Janus particles [47, 48] exposed to extreme confinements [19].

In our model we describe the evolution of active smectics under external confinement based on a continuum density-field theory, i.e., the active PFC model which can be derived from dynamical density functional theory [36, 37] and also from a particle-based microscopic description [42]. It reads

$$\frac{\partial \psi}{\partial t} = \nabla^2 \frac{\delta \mathcal{F}}{\delta \psi} - v_0 \boldsymbol{\nabla} \cdot \mathbf{P}, \tag{1}$$

$$\frac{\partial \mathbf{P}}{\partial t} = \left(\nabla^2 - D_r\right) \frac{\delta \mathcal{F}}{\delta \mathbf{P}} - v_0 \boldsymbol{\nabla} \psi, \tag{2}$$

where ψ is the particle density variation field, the polarization $\mathbf{P}$ represents the local orientation vector field, v_0 measures the strength of particle self-propulsion, and D_r is the rotational diffusion constant. The above dynamical equations have been rescaled, with a diffusive timescale and a length scale set via the pattern periodicity. Here $\mathcal{F} = \mathcal{F}_{\mathrm{aPFC}} + \mathcal{F}_{\mathrm{anch}}$, where $\mathcal{F}_{\mathrm{aPFC}}$ is the free

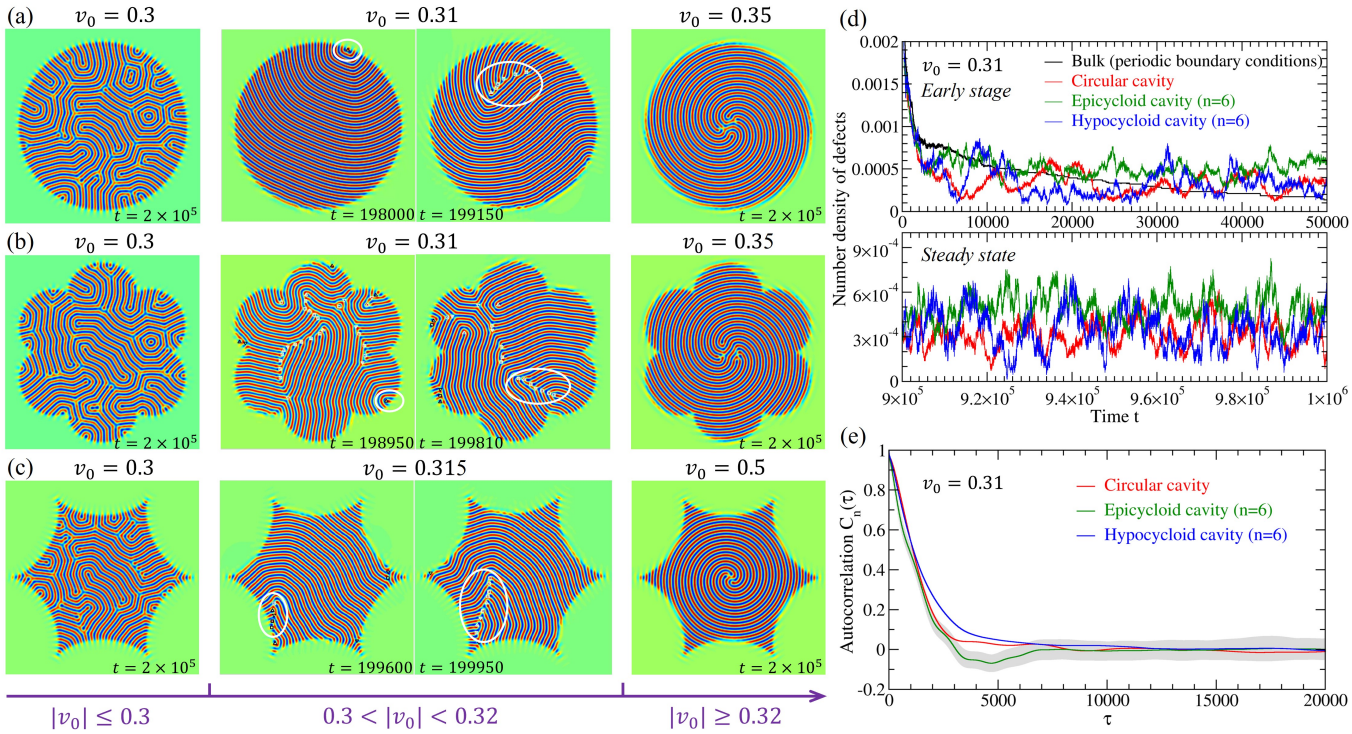

FIG. 1. (a)–(c) Transitions between pinned, highly fluctuating (annihilation-nucleation), and self-rotating defect states with the increase of self-propulsion strength v_0, in (a) circular, (b) epicycloid, and (c) hypocycloid cavities. Each regime is represented by sample simulation snapshots with system size of 256×256 grid points. In the mid panels the circled regions highlight the time-evolving process of boundary-induced defect generation. The bulk defects inside each cavity are labeled by white symbols, and boundary defects by black ones. (d) Sample time variation of number density of defects in the fluctuation regime at $v_0 = 0.31$, for different cavity geometries of 512×512 system size. (e) The corresponding normalized time correlation $C_n(\tau)$ of defect density, calculated over time range $t = 10^5 - 10^6$ and averaged over 80 simulations for each type of cavity. For a better illustration only the error-bar band for epicycloid of $n = 6$ cusps is shown, while those for other cases are of similar range.

energy functional of active PFC [36, 37, 42]

$$\mathcal{F}_{\rm aPFC} = \int d\mathbf{r} \Big\{ \frac{1}{2}\psi \left[\epsilon + \left(\nabla^2 + q_0^2\right)^2\right]\psi - \frac{g}{3}\psi^3 + \frac{1}{4}\psi^4 + \frac{C_1}{2}|\mathbf{P}|^2 + \frac{C_4}{4}|\mathbf{P}|^4 \Big\}, \tag{3}$$

with $\epsilon < 0$ and small magnitude of average density ψ_0 giving rise to the resting or traveling active smectic phase [36], the characteristic wave number $q_0 = 1$ after rescaling, parameters g, C_1, and C_4 that can be expressed via microscopic correlation functions, and $C_1 > 0$ tending to suppress any spontaneous ordering of orientational alignment. We represent the effect of boundary confinement via an anchoring energy

$$\mathcal{F}_{\rm anch} = \int d\mathbf{r} \frac{V_b(\mathbf{r})}{2} \left[(\psi - \psi_b)^2 + |\mathbf{P} - \mathbf{P}_b|^2 + (\hat{\mathbf{n}} \cdot \boldsymbol{\nabla}\psi)^2\right], \tag{4}$$

to effectively satisfy both Dirichlet and Neumann boundary conditions $\psi = \psi_b$, $\mathbf{P} = \mathbf{P}_b$, and $\hat{\mathbf{n}} \cdot \boldsymbol{\nabla}\psi = 0$ (with $\hat{\mathbf{n}}$ the local unit normal) at any implicitly defined domain boundary, with

$$V_b(\mathbf{r}) = \frac{V_{b0}}{2}\left[1 + \tanh\left(\frac{r_s(\mathbf{r})}{\Delta}\right)\right], \tag{5}$$

where V_{b0} gives the anchoring strength, $r_s(\mathbf{r})$ is the signed distance function to the domain boundary (with $r_s < 0$ inside the domain and > 0 outside), and Δ sets the thickness of boundary interface. This approach we develop here combines an approximation of domain interface energy for imposing the boundary conditions and a setup of the diffuse domain method which controls the confinement geometry implicitly through an auxiliary phase field function $\phi(\mathbf{r})$ [49], such that $V_b(\mathbf{r}) = V_{b0}\phi(\mathbf{r})$ here. For more details, including the specific analytical forms for different geometries of the cavities or channels simulated, see Supplemental Material [50]. Equation (4) produces the condition of planar anchoring as found in experiments. Its last term is analogous to the Rapini-Papoular form of surface potential [3, 12]. In our simulations (starting from random initial conditions), we set $(\epsilon, \psi_0, g, D_r, C_1, C_4) = (-0.98, 0, 0, 0.5, 0.2, 0)$ in the strong segregation regime of stripe phase, and $(V_{b0}, \Delta, \psi_b, \mathbf{P}_b) = (1, 0.1, 0, 0)$.

The emergence of topological defects, including disclinations, dislocations, and grain boundaries, is inevitable in large-aspect-ratio systems that are driven out of equilibrium. In the confined cavities of different geometries, our simulation results presented in Fig. 1 show that the evolution of these defects in active smectics is governed by three intrinsically different dynamical regimes and the transitions between them. At weak enough self-propulsion strength v_0 [first column of Figs. 1(a)–1(c)], the stripes (smectic layers) remain perpendicular to the boundary, showing planar anchoring with tangential alignment of constituent particle orientations. The defects emerging from the early stage of system evolution become mostly pinned, with extremely slow local dynamics, similar to the glassy state observed in strongly segregated passive stripe patterns showing no long range orientational order as a result of defect pinning by the pattern-periodicity induced potential barrier [53].

In the other limit of large enough v_0, the particle self-propulsion completely overcomes the defect pinning barrier, facilitating the fast annihilation of defects as accelerated by the effect of self-driving on the smectic layer alignment. As shown in the last column of Figs. 1(a)–1(c), large particle activity also enables the overcoming of boundary anchoring constraint, leading to the violation of local planar anchoring, and depending on the boundary geometry, even to (partially) homeotropic anchoring. At late stage such a strong self-driving induces the rotation of smectics inside the cavity, either clockwise or counterclockwise, and hence the persistent self-rotation of the remaining multi-core spiral defects trapped at the cavity center.

Defect dynamics in these two regimes reveal the competition between rigid boundary confinement restricting the local smectic orientation and the tendency of bulk alignment of stripes [54, 55]. An interesting type of dynamics occurs when such two incompatible boundary and bulk effects are of comparable strength, giving rise to a highly fluctuating state within an intermediate narrow range of active drive v_0 as demonstrated in the mid panels of Figs. 1(a)–1(c). Although the planar boundary anchoring is maintained at very early stage, the deviation occurs at later times as caused by self-propulsion, leading to local distortion of stripes inside the cavity as a result of confinement-alignment competition. Importantly, in addition to the annihilation of defects (including dislocations and disclinations, majorities of which occur at cavity boundaries), new defects can nucleate from the boundary, propagating into the bulk, evolving and generating a subsequence of more new defects like a chain effect, as seen in the circled regions of Fig. 1 and videos of Supplemental Material [50]. This results in the repeated succession of tranquil and active time stages in terms of defect density and dynamics, with some examples for circular and 6-cusp epicycloid and hypocycloid cavities given in Fig. 1(d). In contrast to the fully bulk

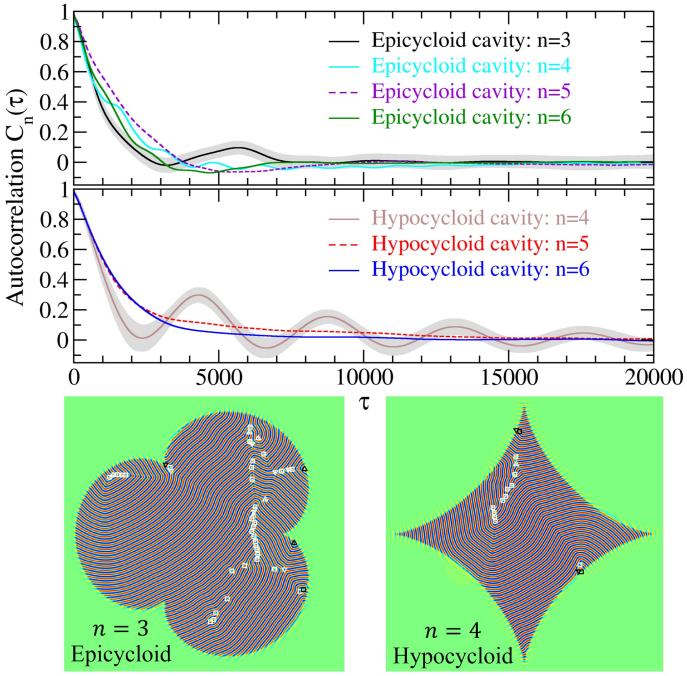

FIG. 2. Autocorrelation function $C_n(\tau)$ of defect number density for various epicycloid and hypocycloid closed cavities at $v_0 = 0.31$. Also shown are two sample snapshots.

state without any boundary confinement (thus with the absence of defect generation) which shows a monotonic time decay of defect number, the cavity confinement induces an intermittency-type behavior with seemingly irregular bursts of number of defects. The boundary cusps appear to enhance the creation of new defects, yielding higher defect density peaks, as compared to the smooth boundary of circular cavity.

The property of this transition zone with dynamical fluctuations of defects can be further quantified through the normalized time autocorrelation function of the defect number density n_d, i.e.,

$$C_n(\tau) = \frac{\langle (n_d(t+\tau) - \langle n_d \rangle)\,(n_d(t) - \langle n_d \rangle) \rangle}{\langle (n_d(t) - \langle n_d \rangle)^2 \rangle}, \quad (6)$$

where the averages are conducted over a long time series in the steady state (e.g., $t = 10^5 - 10^6$ in our calculations) for each simulation run, assuming ergodicity of the corresponding probability measure [25]. Some results of $C_n(\tau)$ are presented in Fig. 1(e), showing a decay behavior for circular and 6-cusp hypocycloid cavities. Interestingly, for epicycloid cavity with $n = 6$ cusps a weak oscillation around a negative minimum correlation (near time scale $\tau_m \sim 5000$) appears, implying a correlated behavior between the burst (active) and low-number (tranquil) regimes of defect density and dynamics.

For a given geometric type of confinement, the behavior of defect autocorrelation can be qualitatively changed through different number of boundary cusps. As shown

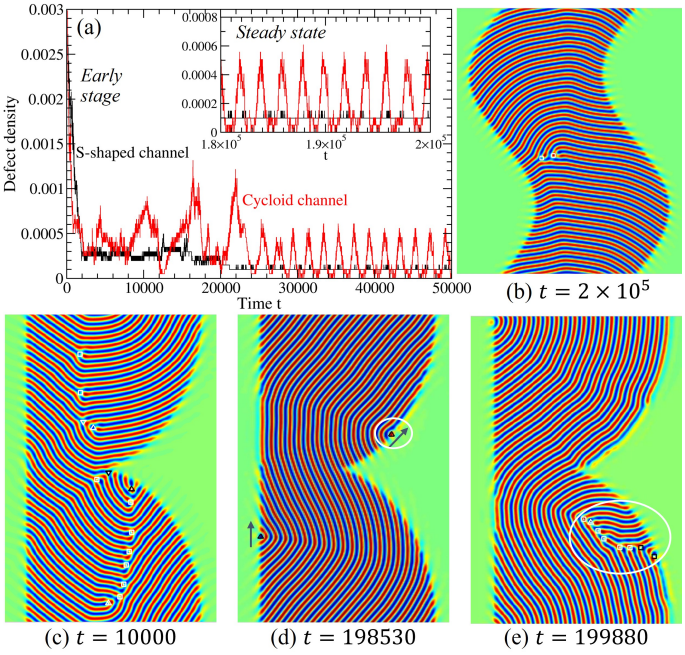

FIG. 3. (a) Time evolution of defect number density in two types of open channels at $v_0 = 0.31$. (b)–(e) Snapshots at different times for (b) S-shaped and (c)–(e) cycloid channels.

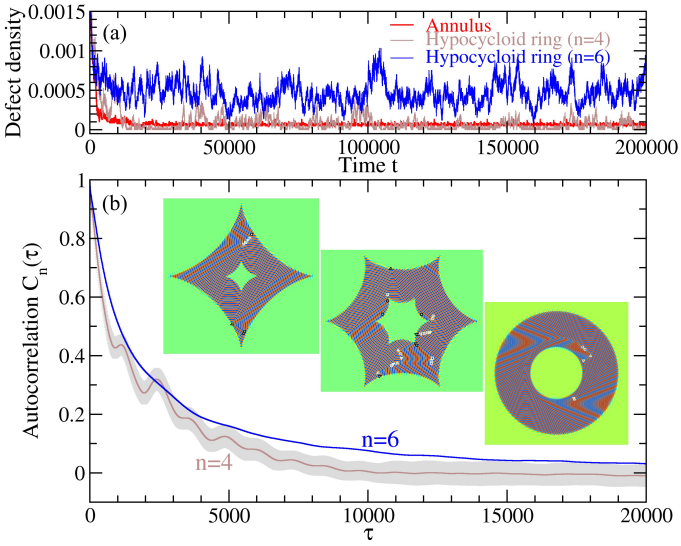

FIG. 4. (a) Time evolution of defect density for three types of closed channels: annulus, $n = 4$ and $n = 6$ hypocycloid rings. (b) Autocorrelation $C_n(\tau)$ (each averaged over 80 runs for $t = 10^5$–10^6) for hypocycloid rings.

in Fig. 2, for epicycloid cavities decreasing the cusp number n from $n = 6$ to 3 leads to the variation of $C_n(\tau)$ minimum from negative to positive correlation. A more dramatic change occurs when lowering the cusp number of hypocycloid cavities. When $n = 5$ and 6 a damped time correlation of defect density is observed, while the $n = 4$ (i.e., astroid) cavity is featured by an oscillatory behavior (within the statistical error) of time correlation, indicating a cyclic state of defect density variation with periodic creation and annihilation of defects over a characteristic time period $\tau_T \sim 4300$. In this cyclic defect dynamics, although generally the spatial locations of boundary defect nucleation and annihilation seem uncorrelated, statistically the periodicity in autocorrelation $C_n(\tau)$ can be attributed to the propagation of defects between different sides of boundary within the defect creation-annihilation time interval (see Video S5 of Supplemental Material).

To further understand the mechanism of defect creation and correlation and hence the accessibility for steering defect dynamics, we examine the process of defect flow in two types of open channels, the S-shaped channel with smooth boundary and the cycloid channel with a single cusp (see Fig. 3, noting the periodic boundary condition along the vertical open ends). No new defects are nucleated from the smooth boundary of S-shaped channel and the defect number decreases with time, with few left at late stage, as seen in Figs. 3(a) and 3(b). In contrast, during the flow of stripes in the cycloid channel [Figs. 3(c)–3(e)], the cusp singularity enhances the local distortion of the smectic layers, thus enabling the formation of defects at boundary (not necessarily at the cusp location). Further distortion during flow can facilitate the defect motion into the bulk and induce a chain of new defects [see Fig. 3(e)]. This burst of defects will be diminished due to their annihilation when traveling to the channel boundary, with few or none remained. After then the similar nucleation-propagation-annihilation process repeats, resulting in the periodic variation of defect number density as shown in Fig. 3(a).

In the confined cavities studied above, the enclosure constraint (without open ends), competing with self-propelled alignment and domain flow in the bulk of large enough aspect ratio, leads to a higher degree of local pattern distortion which enables the defect nucleation at boundary even for no-cusp, circular cavity (see Fig. 1). The mechanism originated from cusp singularity of confinement would play a key role on enhancing defect generation, and importantly, on controlling the time-correlated property of defect variations, including the oscillatory behavior of defect correlation for cavities of small number of cusps as observed in simulations. The oscillation of time correlation function would be damped, and thus the degree of defect periodic variation be reduced, when the cusp number increases as a result of the interference between the effects induced by different individual cusps. This interference effect can account for the transition from oscillatory to non-oscillatory decay of the correlation shown in Fig. 2. In the other limit of zero cusp without the oscillatory mechanism, such as the circular cavity, faster decay of correlation is found [Fig. 1(e)]. Thus, the mechanism generated by cusp singularity provides an effective route for controlling the behavior of

defect dynamics and correlation.

Applying this mechanism, one can expect that further confining via both inner and outer boundaries with same type of topology, i.e., a closed channel with a void, would result in the damping of correlation due to greater constraint with more cusps interference, as verified in Fig. 4 for the $n = 4$ hypocycloid ring. On the other hand, the confinement of closed channel leads to the increase of the correlation time as compared to the closed cavity, as seen from the $C_n(\tau)$ plots for $n = 6$ hypocycloid cavity vs ring in Figs. 2 and 4. In comparison, for annulus with smooth boundary, no new defects can be created, analogous to the case of smooth S-shaped channel.

In summary, we have examined the dynamics of topological defects in active smectic systems subjected to three types of boundary confinements, i.e., closed cavities, open and closed channels with various geometries. Our simulations based on active PFC modeling indicate a viable way to effectively control or steer the complex defect dynamics through both particle self-driving and the topology of extreme confinement. These confined nonequilibrium systems are featured by transitions between three distinct regimes of active and persistent defect dynamics, including defect pinning in a glassy state with ultraslow evolution, the fast self-rotating of centralized spiral defects, and interestingly, a dynamical state governed by far-from-equilibrium, nonrelaxational processes with huge defect fluctuations. For the latter, a key factor is the intermittent but perpetual creation of new defects as enabled by the confinement boundary and enhanced by cuspate boundary topology. A transition from random to time-periodic process of defects creation and annihilation can be made possible through the control of boundary cusp singularity as the mechanism of confinement-induced defect generation. These predictions can be examined and achieved in experiments on dense self-propelled rods [56] which form an active smectic phase. Examples range from vibrated granular rods which can be exposed to circular [44], epicycloid-like flower-shaped [45] or annular [46] confinements, to active colloidal rods [47, 48] in channels and cavities.

Z.-F.H. acknowledges support from the National Science Foundation under Grant No. DMR-2006446. H.L. and A.V. were supported by the German Research Foundation (DFG) via projects LO 418/20-2 and VO 899/19-2.

[1] P. M. Chaikin and T. C. Lubensky, *Principles of Condensed Matter Physics* (Cambridge University Press, 1995).

[2] P.-G. de Gennes and J. Prost, *The Physics Of Liquid Crystals* (Clarendon Press, 1993).

[3] M. Kleman and O. D. Lavrentovich, *Soft Matter Physics - An Introduction* (Springer-Verlag, 2003).

[4] Y. Reznikov, O. Ostroverkhova, K. D. Singer, J.-H. Kim, S. Kumar, O. Lavrentovich, B. Wang, and J. L. West, Photoalignment of liquid crystals by liquid crystals, Phys. Rev. Lett. **84**, 1930 (2000).

[5] Y. D. Gu and N. L. Abbott, Observation of Saturn-ring defects around solid microspheres in nematic liquid crystals, Phys. Rev. Lett. **85**, 4719 (2000).

[6] H. Stark, Saturn-ring defects around microspheres suspended in nematic liquid crystals: An analogy between confined geometries and magnetic fields, Phys. Rev. E **66**, 032701 (2002).

[7] P. E. Cladis, W. van Saarloos, P. L. Finn, and A. R. Kortan, Dynamics of line defects in nematic liquid crystals, Phys. Rev. Lett. **58**, 222 (1987).

[8] D. R. Link, J. E. Maclennan, and N. A. Clark, Simultaneous observation of electric field coupling to longitudinal and transverse ferroelectricity in a chiral liquid crystal, Phys. Rev. Lett. **77**, 2237 (1996).

[9] O. D. Lavrentovich, Phase transition altering the symmetry of topological point defects (hedgehogs) in a nematic liquid crystal, Zh. Eksp. Teor. Fiz. **91**, 2084 (1986).

[10] O. J. Dammone, I. Zacharoudiou, R. P. A. Dullens, J. M. Yeomans, M. P. Lettinga, and D. G. A. L. Aarts, Confinement induced splay-to-bend transition of colloidal rods, Phys. Rev. Lett. **109**, 108303 (2012).

[11] Y. Trukhina and T. Schilling, Computer simulation study of a liquid crystal confined to a spherical cavity, Phys. Rev. E **77**, 011701 (2008).

[12] O. V. Manyuhina, K. B. Lawlor, M. C. Marchetti, and M. J. Bowick, Viral nematics in confined geometries, Soft Matter **11**, 6099 (2015).

[13] P. E. Brumby, H. H. Wensink, A. J. Haslam, and G. Jackson, Structure and interfacial tension of a hard-rod fluid in planar confinement, Langmuir **33**, 11754 (2017).

[14] I. C. Gârlea, P. Mulder, J. Alvarado, O. J. Dammone, D. G. A. L. Aarts, M. P. Lettinga, G. H. Koenderink, and B. M. Mulder, Finite particle size drives defect-mediated domain structures in strongly confined colloidal liquid crystals, Nat. Commun. **7**, 12112 (2016).

[15] M. Kléman and O. D. Lavrentovich, Grain boundaries and the law of corresponding cones in smectics, Euro. Phys. J. E **2**, 47 (2000).

[16] B. G.-g. Chen, G. P. Alexander, and R. D. Kamien, Symmetry breaking in smectics and surface models of their singularities, Proc. Natl. Acad. Sci. U.S.A. **106**, 15577 (2009).

[17] D. B. Liarte, M. Bierbaum, R. A. Mosna, R. D. Kamien, and J. P. Sethna, Weirdest martensite: Smectic liquid crystal microstructure and Weyl-Poincaré invariance, Phys. Rev. Lett. **116**, 147802 (2016).

[18] J. Jeong and M. W. Kim, Confinement-induced transition of topological defects in smectic liquid crystals: From a point to a line and pearls, Phys. Rev. Lett. **108**, 207802 (2012).

[19] R. Wittmann, L. B. G. Cortes, H. Löwen, and D. G. A. L. Aarts, Particle-resolved topological defects of smectic colloidal liquid crystals in extreme confinement, Nat. Commun. **12**, 623 (2021).

[20] P. A. Monderkamp, R. Wittmann, L. B. G. Cortes, D. G. A. L. Aarts, F. Smallenburg, and H. Löwen, Topology of orientational defects in confined smectic liquid crystals, Phys. Rev. Lett. **127**, 198001 (2021).

[21] M. C. Marchetti, J. F. Joanny, S. Ramaswamy, T. B. Liverpool, J. Prost, M. Rao, and R. A. Simha, Hydrody-

namics of soft active matter, Rev. Mod. Phys. **85**, 1143 (2013).
[22] C. Bechinger, R. Di Leonardo, H. Löwen, C. Reichhardt, G. Volpe, and G. Volpe, Active particles in complex and crowded environments, Rev. Mod. Phys. **88**, 045006 (2016).
[23] J. Berry, C. P. Brangwynne, and M. Haataja, Physical principles of intracellular organization via active and passive phase transitions, Rep. Prog. Phys. **81**, 046601 (2018).
[24] M. J. Bowick, N. Fakhri, M. C. Marchetti, and S. Ramaswamy, Symmetry, thermodynamics, and topology in active matter, Phys. Rev. X **12**, 010501 (2022).
[25] M. C. Cross and P. C. Hohenberg, Pattern formation outside of equilibrium, Rev. Mod. Phys. **65**, 851 (1993).
[26] S. P. Thampi, R. Golestanian, and J. M. Yeomans, Instabilities and topological defects in active nematics, Europhys. Lett. **105**, 18001 (2014).
[27] S. P. Thampi, R. Golestanian, and J. M. Yeomans, Vorticity, defects and correlations in active turbulence, Phil. Trans. Roy. Soc. A **372**, 20130366 (2014).
[28] G. Duclos, C. Erlenkamper, J.-F. Joanny, and P. Silberzan, Topological defects in confined populations of spindle-shaped cells, Nat. Phys. **13**, 58 (2017).
[29] T. B. Saw, A. Doostmohammadi, V. Nier, L. Kocgozlu, S. Thampi, Y. Toyama, P. Marcq, C. T. Lim, J. M. Yeomans, and B. Ladoux, Topological defects in epithelia govern cell death and extrusion, Nature **544**, 212 (2017).
[30] A. Doostmohammadi, J. Ignes-Mullol, J. M. Yeomans, and F. Sagues, Active nematics, Nat. Comm. **9**, 3246 (2018).
[31] R. Keogh, S. Chandragiri, B. Loewe, T. Ala-Nissila, S. Thampi, and T. N. Shendruk, Helical flow states in active nematics, arXiv:2112.01393 (2021).
[32] L. Chen and J. Toner, Universality for Moving Stripes: A Hydrodynamic Theory of Polar Active Smectics, Phys. Rev. Lett. **111**, 088701 (2013).
[33] P. Romanczuk, H. Chate, L. Chen, S. Ngo, and J. Toner, Emergent smectic order in simple active particle models, New J. Phys. **18**, 063015 (2016).
[34] S. Saha, J. Agudo-Canalejo, and R. Golestanian, Scalar active mixtures: The nonreciprocal Cahn-Hilliard model, Phys. Rev. X **10**, 041009 (2020).
[35] S. Tarama, S. U. Egelhaaf, and H. Löwen, Traveling band formation in feedback-driven colloids, Phys. Rev. E **100**, 022609 (2019).
[36] A. M. Menzel and H. Löwen, Traveling and resting crystals in active systems, Phys. Rev. Lett. **110**, 055702 (2013).
[37] A. M. Menzel, T. Ohta, and H. Löwen, Active crystals and their stability, Phys. Rev. E **89**, 022301 (2014).
[38] F. Alaimo, S. Praetorius, and A. Voigt, A microscopic field theoretical approach for active systems, New J. Phys. **18**, 083008 (2016).
[39] F. Alaimo and A. Voigt, Microscopic field-theoretical approach for mixtures of active and passive particles, Phys. Rev. E **98**, 032605 (2018).
[40] S. Praetorius, A. Voigt, R. Wittkowski, and H. Löwen, Active crystals on a sphere, Phys. Rev. E **97**, 052615 (2018).
[41] L. Ophaus, S. V. Gurevich, and U. Thiele, Resting and traveling localized states in an active phase-field-crystal model, Phys. Rev. E **98**, 022608 (2018).
[42] Z.-F. Huang, A. M. Menzel, and H. Löwen, Dynamical crystallites of active chiral particles, Phys. Rev. Lett. **125**, 218002 (2020).
[43] L. Ophaus, E. Knobloch, S. V. Gurevich, and U. Thiele, Two-dimensional localized states in an active phase-field-crystal model, Phys. Rev. E **103**, 032601 (2021).
[44] V. Narayan, N. Menon, and S. Ramaswamy, Nonequilibrium steady states in a vibrated-rod monolayer: tetratic, nematic, and smectic correlations, J. Stat. Mech: Theory Exp. **2006**, P01005 (2006).
[45] J. Deseigne, O. Dauchot, and H. Chaté, Collective motion of vibrated polar disks, Phys. Rev. Lett. **105**, 098001 (2010).
[46] A. D.-D. Armas, M. Maza-Cuello, Y. Martínez-Ratón, and E. Velasco, Domain walls in vertically vibrated monolayers of cylinders confined in annuli, Phys. Rev. Research **2**, 033436 (2020).
[47] H. R. Vutukuri, Z. Preisler, T. H. Besseling, A. van Blaaderen, M. Dijkstra, and W. T. S. Huck, Dynamic self-organization of side-propelling colloidal rods: experiments and simulations, Soft Matter **12**, 9657 (2016).
[48] M. S. Davies Wykes, J. Palacci, T. Adachi, L. Ristroph, X. Zhong, M. D. Ward, J. Zhang, and M. J. Shelley, Dynamic self-assembly of microscale rotors and swimmers, Soft Matter **12**, 4584 (2016).
[49] X. Li, J. Lowengrub, A. Ratz, and A. Voigt, Solving PDEs in complex geometries: A diffuse domain approach, Commun. Math. Sci. **7**, 81 (2009).
[50] See Supplemental Material for the detailed setup of various types of boundary geometries, the algorithm used for defect detection, and simulation videos of defect dynamics for confined active smectics, which includes Refs. [51, 52].
[51] H. Qian and G. F. Mazenko, Defect structures in the growth kinetics of the Swift-Hohenberg model, Phys. Rev. E **67**, 036102 (2003).
[52] C. Harrison, *Block copolymer microdomains in thin films*, Ph.D. thesis, Princeton University (1999).
[53] D. Boyer and J. Viñals, Grain boundary pinning and glassy dynamics in stripe phases, Phys. Rev. E **65**, 046119 (2002).
[54] M. C. Cross, Ingredients of a theory of convective textures close to onset, Phys. Rev. A **25**, 1065 (1982).
[55] H. S. Greenside and W. M. Coughran, Nonlinear pattern formation near the onset of Rayleigh-Bénard convection, Phys. Rev. A **30**, 398 (1984).
[56] M. Bär, R. Großmann, S. Heidenreich, and F. Peruani, Self-propelled rods: Insights and perspectives for active matter, Annu. Rev. Condens. Matter Phys. **11**, 441 (2020).

Supplemental Material
Defect Dynamics in Active Smectics Steered by Extreme Confinement

Zhi-Feng Huang,[1] Hartmut Löwen,[2] and Axel Voigt[3]

[1] *Department of Physics and Astronomy, Wayne State University, Detroit, MI 48201, USA*
[2] *Institut für Theoretische Physik II: Soft Matter, Heinrich-Heine-Universität Düsseldorf, 40225 Düsseldorf, Germany*
[3] *Institute of Scientific Computing, Technische Universität Dresden, 01062 Dresden, Germany*

I. CONFINEMENT GEOMETRIES

As described in Eqs. (4) and (5) of the main text, to implement the planar anchoring condition of boundary confinement we develop an approach by combining a formulation of surface/interface free energy for imposing the rigid boundary conditions (i.e., $\psi = \psi_b$, $\hat{\mathbf{n}} \cdot \boldsymbol{\nabla}\psi = 0$, and $\mathbf{P} = \mathbf{P}_b$, with ψ_b and $\mathbf{P}_b$ the boundary values of density field ψ and orientation field $\mathbf{P}$), with the control of confinement geometry via the spatially dependent interface energy amplitude $V_b(\mathbf{r}) = V_{b0}\phi(\mathbf{r})$, where V_{b0} is the anchoring strength. Here $\phi(\mathbf{r})$ is an auxiliary phase field function and in the diffuse domain method [S1] is approximated as

$$\phi(\mathbf{r}) = \frac{1}{2}\left[1 + \tanh\left(\frac{r_s(\mathbf{r})}{\Delta}\right)\right], \tag{S1}$$

where Δ is the interface width of the boundary and $r_s(\mathbf{r})$ is the signed distance function from any location $\mathbf{r}$ to the domain boundary $\partial\Omega$. $r_s(\mathbf{r}) = -d(\mathbf{r}) < 0$ inside the domain Ω and $r_s(\mathbf{r}) = d(\mathbf{r}) > 0$ outside Ω, with $d(\mathbf{r})$ the distance function to $\partial\Omega$. Various methods or algorithms for calculating signed distance functions have been available. For 2D domain boundaries studied here, we can directly obtain analytic forms of r_s for some simple geometries (see below). In the cases of complex boundary geometries, a straightforward way of approximation, as used in our simulations, is to numerically compute the distances $d_i = |\mathbf{r} - \mathbf{r}_{bi}|$ to the points $\mathbf{r}_{bi} \in \partial\Omega$ $(i = 1, 2, ...)$ discretized on the boundary curve and find the shortest distance among them, i.e.,

$$d(\mathbf{r}) = \min(d_i(\mathbf{r})) = \min_{\mathbf{r}_{bi}\in\partial\Omega}(|\mathbf{r} - \mathbf{r}_{bi}|), \tag{S2}$$

which also determines the boundary point $\mathbf{r}_b$ corresponding to each $\mathbf{r}$. The local unit normal to the boundary is then

$$\hat{\mathbf{n}} = (\mathbf{r} - \mathbf{r}_b)/d(\mathbf{r}). \tag{S3}$$

The following types of confinement geometries have been examined in our simulations:

(i) *Circular cavity and annulus*: For a 2D circular cavity of radius r_0, with cavity center located at $\mathbf{r}_c = (x_c, y_c)$, we have $|\mathbf{r}| = r = [(x - x_c)^2 + (y - y_c)^2]^{1/2}$, $\hat{\mathbf{n}} = \hat{\mathbf{r}}$, $r_s = r - r_0$, and

$$\phi(\mathbf{r}) = \frac{1}{2}\left[1 + \tanh\left(\frac{r - r_0}{\Delta}\right)\right]. \tag{S4}$$

For an annulus with inner and outer radius of $r_{\rm in}$ and $r_{\rm out}$ respectively, $\hat{\mathbf{n}} = \hat{\mathbf{r}}$ and

$$\phi(\mathbf{r}) = \frac{1}{2}\left\{1 + \tanh\left[\frac{|r - (r_{\rm in} + r_{\rm out})/2| - (r_{\rm out} - r_{\rm in})/2}{\Delta}\right]\right\}. \tag{S5}$$

(ii) *S-shaped open channel*: Assume the channel is aligned vertically, with its center at $\mathbf{r}_c = (x_c, y_c)$ and the average locations of right and left boundaries at $x - x_c = \pm x_0$. The boundary curves are of the form

$$x_b = x_c \pm x_0 - S_0 \sin[q_s(y - y_c)], \tag{S6}$$

where S_0 is the amplitude and $2\pi/q_s$ is the periodicity of the S-shaped modulation. The boundary normal is given by

$$\hat{\mathbf{n}} = \frac{(-1, dx/dy)}{\sqrt{1 + (dx/dy)^2}} = \frac{(-1, -q_s S_0 \cos[q_s(y - y_c)])}{\sqrt{1 + q_s^2 S_0^2 \cos^2[q_s(y - y_c)]}}. \tag{S7}$$

The area of this open channel in a system of vertical length l_y is equal to $2x_0 l_y$ (when l_y is set as an integer number of modulation periodicity), which is used in the calculation of defect number density. The corresponding phase field function is approximated by

$$\phi(\mathbf{r}) \simeq \frac{1}{2}\left[1+\tanh\left(\frac{|x-x_c|-|x_b|}{\Delta}\right)\right]. \tag{S8}$$

Note that although $r_s \neq |x-x_c|-|x_b|$ for this S-shaped channel, the above equation is still a good approximation for $\phi(\mathbf{r})$ when Δ is small enough (i.e., for sharp boundary interface).

(iii) *Epicycloid cavities with n cusps*: The corresponding parametric equations are given by

$$\begin{aligned} x &= (a+b)\cos\theta - b\cos\left(\frac{a+b}{b}\theta\right), \\ y &= (a+b)\sin\theta - b\sin\left(\frac{a+b}{b}\theta\right), \end{aligned} \tag{S9}$$

where the parameter θ (not the polar angle) ranges from 0 to 2π, and $b = a/n$ for a n-cusped epicycloid. The area of the enclosed cavity is $(n+1)(n+2)\pi b^2$ for integer n. The related phase field function $\phi(\mathbf{r})$ is calculated via Eq. (S1) with $r_s(\mathbf{r})$ and the unit normal $\hat{\mathbf{n}}$ identified numerically as described above. Some sample results obtained from our simulations are presented in the main text and supplemental Videos S1–S4 for different cusp number n, including $n = 3$ (of shape similar to trefoil), 4 (similar to quatrefoil), 5 (ranunculoid), and 6.

(iv) *Hypocycloid cavities and rings*: For a hypocycloid cavity with n cusps, the parametric equations are written as

$$\begin{aligned} x &= (a-b)\cos\theta + b\cos\left(\frac{a-b}{b}\theta\right), \\ y &= (a-b)\sin\theta - b\sin\left(\frac{a-b}{b}\theta\right), \end{aligned} \tag{S10}$$

where $b = a/n$. The cavity area is equal to $(n-1)(n-2)\pi b^2$. At each position inside or outside of cavity, values of phase field function ϕ, r_s, and $\hat{\mathbf{n}}$ are computed numerically by following the above procedure. Some sample simulation results for $n = 4$ (astroid), 5, and 6 hypocycloid cavities are given in the main text and Videos S5–S7. Similar setup can be used for hypocycloid rings, with inner and outer boundary curves each determined by the above parametric equations with two sets of a and b parameters (see some sample simulation snapshots given in Fig. 4 of the main text and Video S8).

(v) *Cycloid open channel*: For a vertically aligned channel, the left boundary is a straight line located at $x = -x_1$ (so that $r_s = \pm|x+x_1|$ and $\hat{\mathbf{n}} = (1,0)$), while the right boundary curve is of a cycloid or trochoid form described by

$$\begin{aligned} x &= a - b\cos\theta + x_0, \\ y &= a\theta - b\sin\theta. \end{aligned} \tag{S11}$$

It is a curtate cycloid if $a > b$, a prolate cycloid if $a < b$, and a cycloid when $a = b$ which is used in our simulations. We choose $-\pi \leq \theta \leq \pi$ and set $2\pi a = l_y$ to satisfy the periodic boundary condition along the y direction with open ends of the channel. The corresponding channel area is equal to $\pi(2a^2+b^2)+2\pi a(x_0+x_1)$. This channel configuration is implemented in our simulations through numerical calculations of ϕ, r_s, and $\hat{\mathbf{n}}$, with examples given in Fig. 3 of the main text.

In principle any other types of boundary geometries, as long as the corresponding analytic or numerical expressions of boundary curves are available, can be described via similar procedure and thus implemented in our modeling and simulations. This approach that we introduce here, based on Eqs. (4) and (5) of the main text and the above implicit representation of domain boundary, allows us to apply the pseudospectral method with periodic boundary conditions in the whole system to numerically solve the active PFC equations subjected to the confinement of various types of cavity or channel geometry.

II. ALGORITHM FOR DEFECT DETECTION

To identify the topological defects (dislocations, disclinations, and grain boundaries) in the simulated smectic pattern, we use an algorithm based on the combination of two methods given in Refs. [S2, S3], with some modifications and extension. The implementation steps are described below.

Given the local stripe orientation $\hat{\mathbf{n}}_s = \boldsymbol{\nabla}\psi/|\boldsymbol{\nabla}\psi| = (\cos\theta_s, \sin\theta_s)$ with θ_s the local orientation angle of the smectic layer, we can calculate at each spatial location $\mathbf{r} = (x, y)$

$$|\boldsymbol{\nabla}\psi|^2 \sin 2\theta_s = 2(\partial_x\psi)(\partial_y\psi), \qquad |\boldsymbol{\nabla}\psi|^2 \cos 2\theta_s = (\partial_x\psi)^2 - (\partial_y\psi)^2. \tag{S12}$$

Then a Gaussian smoothing of each of $|\boldsymbol{\nabla}\psi|^2 \sin 2\theta_s$ and $|\boldsymbol{\nabla}\psi|^2 \cos 2\theta_s$ is conducted over a neighboring square range of grid points for each position $\mathbf{r}$ [S3], and the local director orientation is identified by

$$\theta_s = \frac{1}{2} \arctan\left[\frac{\left(|\boldsymbol{\nabla}\psi|^2 \sin 2\theta_s\right)_{\text{smoothed}}}{\left(|\boldsymbol{\nabla}\psi|^2 \cos 2\theta_s\right)_{\text{smoothed}}}\right]. \tag{S13}$$

To detect the locations of defect cores, at each grid point the local orientation gradient is calculated [S2], i.e.,

$$A_s = |\boldsymbol{\nabla}\theta_s|^2. \tag{S14}$$

If A_s exceeds a threshold value A_{0s} (e.g., $A_{0s} = 0.2/(\Delta x)^2$, with $\Delta x = \pi/4$ the numerical grid spacing), the corresponding grid point is considered to be in a defect core region. To obtain the specific location of each individual defect core, first the individual cluster of sites for each defect core region is identified by using the Hoshen-Kopelman (Union-Find) algorithm with raster scan to connect neighboring grid points of each cluster tree with large enough local orientation variation ($A_s > A_{0s}$). The cluster's center of mass then gives the position $\mathbf{r}_{\text{CM}}$ of the corresponding defect core, with

$$\mathbf{r}_{\text{CM}} = \frac{\sum_j \mathbf{r}_j A_s(\mathbf{r}_j)}{\sum_j A_s(\mathbf{r}_j)}, \tag{S15}$$

where $\mathbf{r}_j$ is the spatial coordinate of site j within the cluster.

To reduce the artifacts or ambiguities caused by the choice of threshold A_{0s}, if the size of a cluster is larger than a limit (e.g., 20 grid sites) this part is then re-clustered through the Union-Find algorithm to divide it into smaller sub-clusters by increasing its threshold value A_{0s} by a percentage (e.g., 1/8) of $\max(A_s) - \min(A_s)$ of that cluster. In addition, if the distance between the centers of mass $\mathbf{r}_{\text{CM}}$ of any two clusters is less than another threshold value (e.g., $5.5\Delta x$), they will be merged if the merged/connected cluster size would not exceed an upper limit (e.g., 18 sites). This reclustering-merging process is conducted only once, and the corresponding defect core locations (i.e., cluster centers of mass) will be recalculated.

To identify the specific type of each individual defect, we follow the standard procedure of calculating the topological charge (winding number) of each defect core by performing a closed-path integral of θ_s over a counterclockwise square loop around the position of defect core [S2, S3]. The defect type (charge-0 dislocation vs $\pm 1/2$ disclination) is determined via the calculated value of topological charge. It is noted that all the above calculations are for the orientation of stripes (determined by the apolar density field ψ) and the corresponding topological charges, but not for the polar vector field $\mathbf{P}$ which would yield different topological charges via a similar procedure of calculation. A boundary defect is labeled if the location of its defect core is within a certain distance (e.g., 8 grid points) to the cavity or channel boundary. We can also identify the defect cores (clusters) belonging to a grain boundary (cluster chain), via the Union-Find algorithm again (but not merging them), if the distance between the centers of mass ($\mathbf{r}_{\text{CM}}$) of any two clusters (defect cores) is less than or equal to a value (e.g., $25\Delta x$) and if there are at least N_{GB} (e.g., $= 4$) of such clusters (cores).

There would still be some ambiguities/uncertainties of defect identification, which are unavoidable for any detection algorithm particularly for the cases of close or crowded defect cores. We have checked the results by varying different parameters of the algorithm and comparing with some manual spot checks to identify the (close-to) optimal or compromised choices of parameters, and to ensure the results are consistent statistically.

III. SUPPLEMENTAL VIDEOS

- Video S1: Simulation video of defect dynamics (including defect traveling, generation, and annihilation) for $n = 3$ epicycloid closed cavity at $v_0 = 0.31$, during a time range from $t = 198000$ to $t = 200000$ with 512×512 system size.
- Video S2: Simulation video of defect dynamics (including defect traveling, generation, and annihilation) for $n = 4$ epicycloid closed cavity at $v_0 = 0.31$, during a time range from $t = 198000$ to $t = 200000$ with 512×512 system size.

- Video S3: Simulation video of defect dynamics (including defect traveling, generation, and annihilation) for $n = 5$ epicycloid (ranunculoid) closed cavity at $v_0 = 0.31$, during a time range from $t = 198000$ to $t = 200000$ with 512×512 system size.
- Video S4: Simulation video of defect dynamics (including defect traveling, generation, and annihilation) for $n = 6$ epicycloid closed cavity at $v_0 = 0.31$, during a time range from $t = 198000$ to $t = 200000$ with 512×512 system size.
- Video S5: Simulation video of defect dynamics (including defect traveling, generation, and annihilation) for $n = 4$ hypocycloid (astroid) closed cavity at $v_0 = 0.31$, during a time range from $t = 195000$ to $t = 198250$ with 512×512 system size.
- Video S6: Simulation video of defect dynamics (including defect traveling, generation, and annihilation) for $n = 5$ hypocycloid closed cavity at $v_0 = 0.31$, during a time range from $t = 198000$ to $t = 200000$ with 512×512 system size.
- Video S7: Simulation video of defect dynamics (including defect traveling, generation, and annihilation) for $n = 6$ hypocycloid closed cavity at $v_0 = 0.31$, during a time range from $t = 198000$ to $t = 200000$ with 512×512 system size.
- Video S8: Simulation video of defect dynamics (including defect traveling, generation, and annihilation) for $n = 6$ hypocycloid ring (closed channel) at $v_0 = 0.31$, during a time range from $t = 198000$ to $t = 200000$ with 512×512 system size.

[S1] X. Li, J. Lowengrub, A. Ratz, and A. Voigt, Solving PDEs in complex geometries: A diffuse domain approach, Commun. Math. Sci. **7**, 81 (2009).
[S2] H. Qian and G. F. Mazenko, Defect structures in the growth kinetics of the Swift-Hohenberg model, Phys. Rev. E **67**, 036102 (2003).
[S3] C. Harrison, *Block copolymer microdomains in thin films*, Ph.D. thesis, Princeton University (1999).